

URTeC: 3723523

Deriving Elastic and Petrophysical Properties from Small Sample Volumes Using Digital Rock Analysis

Vegar Ravlo*¹, Pål-Eric Øren², Cathrine Ringstad³, 1. Petricore USA, 2. Petricore Norway, 3. SINTEF AS.

Copyright 2022, Unconventional Resources Technology Conference (URTeC) DOI 10.15530/urtec-2022-3723523

This paper was prepared for presentation at the Unconventional Resources Technology Conference held in Houston, Texas, USA, 20-22 June 2022.

The URTeC Technical Program Committee accepted this presentation on the basis of information contained in an abstract submitted by the author(s). The contents of this paper have not been reviewed by URTeC and URTeC does not warrant the accuracy, reliability, or timeliness of any information herein. All information is the responsibility of, and, is subject to corrections by the author(s). Any person or entity that relies on any information obtained from this paper does so at their own risk. The information herein does not necessarily reflect any position of URTeC. Any reproduction, distribution, or storage of any part of this paper by anyone other than the author without the written consent of URTeC is prohibited.

Abstract

In this technical paper we describe a robust methodology for performing advanced analysis on smaller sample volumes from unconventional reservoirs. The described methodology incorporates a multi-scale and multi-modal imaging workflow where scanning electron microscopy and spatial mineralogy are used for rock characterization, followed by acquisition of 3D volumes with nanometer resolution for pore scale analysis and generation of digital 3D models.

The presence of pore-backs, an artefact often observed in focused ion beam scanning electron microscopy (FIB-SEM) images, demands a refinement of existing image segmentation workflows to obtain a representative characterization of mineral phases and pore space. Traditional segmentation techniques are combined with trainable segmentation tools that applies machine learning algorithms to identify material phases based on morphological properties. The resulting segmented 3D volumes are transformed into a geometrically accurate pore network model retaining the essential features of the pore space, which allows for simulations of rock properties on a digital rock model. Digital rock models allow for the extraction of local trends in cross-correlated properties through sub-volume calculations.

The concept of a common rock model, where multi-disciplinary properties are calculated on the same model, facilitates a comprehensive rock characterization in despite the physically small sample. Elastic properties were calculated in addition to basic petrophysical properties, and comparisons with laboratory data as well as literature data have been conducted to validate the predicted properties. The comparisons show that the results are in good agreement through the range of properties obtained, which is a strong indication that the application of digital rock analysis on small sample volumes, such as drill cuttings, can provide significant information that influences the processes of drilling, hydraulic fracturing, and production of unconventional reservoirs.

Introduction

Understanding the material and transport properties of complex reservoir formations is fundamental for economic production from unconventional systems. The cost of obtaining core samples from the subsurface drives the development of technology to obtain petrophysical and mechanical properties from smaller sized sources like drill cuttings. Conventional laboratory experiments will often face the challenges of requiring large sample sizes, time consumption and accuracy in interpretation. It is also difficult to interpret and evaluate the pore scale, micro-mechanical, behavior of shale rocks. The elastic properties of a shale rock are mainly governed by the relative amount of each present mineral type, the elastic properties of these mineral types, and finally the spatial and geometrical distribution of the respective mineral types.

Digital rock analysis, by imaging the rock micro-structure in 2D and 3D, has the ability to accurately characterize both the relative amount and the spatial and geometrical distribution of the mineral phases in a rock sample. Scanning electron microscopy (SEM), combined with automated spatial mineralogy, captures the relative amount of mineral types, while focused ion beam (FIB) SEM facilitates the characterization of the spatial distribution of the minerals. A multi-scale imaging workflow was applied to identify representative locations for conducting pore scale analysis on 3D datasets.

In addition to elastic properties, petrophysical properties are calculated on pore network models (PNM) extracted from the segmented 3D datasets. The petrophysical properties are obviously important parameters for the rock characterization by itself, but they are also of high interest for evaluating the digital rock characterization through a comparison with laboratory measurements conducted on larger sample sizes.

Sample and sample preparation

The sample analyzed in this study is an outcrop core plug from the Pierre shale, a marine deposit widely distributed east of the Rocky Mountains in the Great Plains. The Pierre shale is of late cretaceous age and consist of dark grey shale with presence of sandy and bentonitic units. Pierre conformably overlies the Niobrara formation and is overlain by the Fox Hills sandstone.

The extracted core plug was stored in mineral oil for preservation until the start of this study. The diameter of the plug was 3.8cm and the length was approximately 1cm. A standard grinding and mechanical polishing method was applied to generate the initial sample surface. Topographic irregularities on this surface, due to differential hardness of components, will reduce the reliability and accuracy of the analyzes from digital images. These topographic irregularities were minimized by ion milling of the surface. Ion milling is a physical etching technique where ions from an inert gas, in this case Argon, are accelerated from a wide beam ion source into the surface under vacuum. The angled bombardment of high energy ions creates a clean and polished surface, which also removes smearing effects observed from mechanical polishing. The ion milled surface is then coated with a thin electrically conductive layer prior to the analysis.

Multiscale imaging

A multiscale imaging workflow was applied to ensure that representative images and analyses were conducted on the sample. Image mosaics, containing tens to hundreds of individual tiles, acquired at higher magnifications are captured within a previously imaged area to bridge the understanding of pore scale features to plug scale features. The ability to identify representative textures, by utilizing a multi-scale imaging approach, is imperative for identifying prime locations for further 3D analysis using Focused Ion Beam SEM (Lemmens et al. [2013]).

The multiscale imaging workflow starts with the acquisition of a scout image, which is a relatively low-magnification image mosaic covering the complete sample surface. The scout image is used for visual inspection of the sample, and to locate a representative area for an overview image which contains the

least amount of induced micro-fractures and anomalies with regards to heterogeneity. The acquired scout image for the sample is a mosaic containing 40 tiles (8x5) with a total horizontal width of 20.9mm, with an image resolution of 1.47 μ m/pix (see Figure 1(a)).

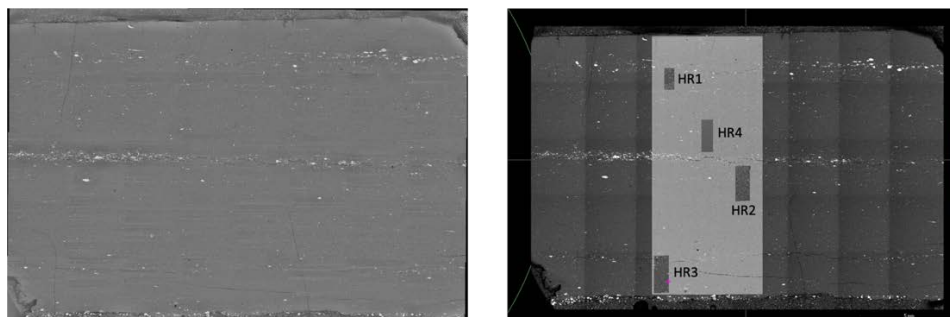


Figure 1: (a) Scout image of the ion milled surface of the Pierre sample. (b) Overview BSE showing the four locations selected for high resolution analysis

As the sample surface is prepared perpendicular to bedding one can observe laminations horizontally in the scout image. The visual inspection of the scout image shows no clear indications of lateral heterogeneities. Hence the overview image is selected to capture the entire vertical section with a rectangular mosaic (8x17 tiles) with 136 individual tiles (see Figure 1 (b)).

Automated spatial mineralogy was acquired in parallel with all SEM mosaics, with the exception of the scout image. Spatial mineralogy couples SEM with energy dispersive X-ray spectrometers to image and mineralogically map samples. Each field is then divided into a virtual grid, the size of which is determined by the vertical and horizontal pixel spacings.

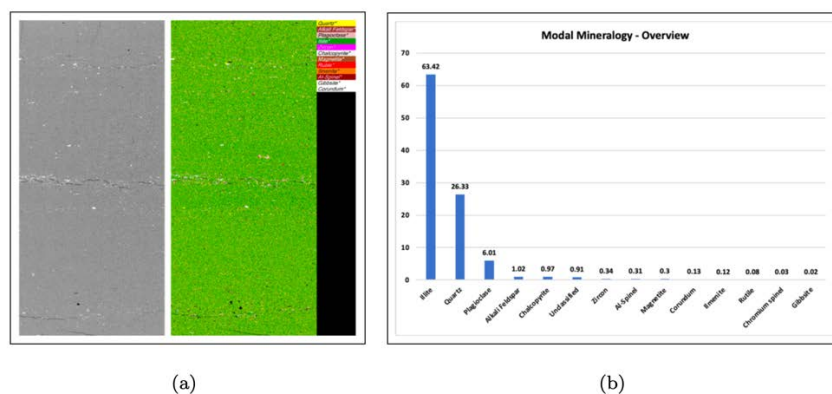


Figure 2: (a) Overview BSEM (left) and false colored mineralogy map (right). (b) Modal mineralogy from automated spatial mineralogy. Values in area percentages.

Inspection of the overview image shows similar properties throughout the sample depth, except for a few thin layers with elevated amounts of heavy minerals. The four high resolution image mosaics are acquired away from these pyrite-rich laminae (see Figure 1).

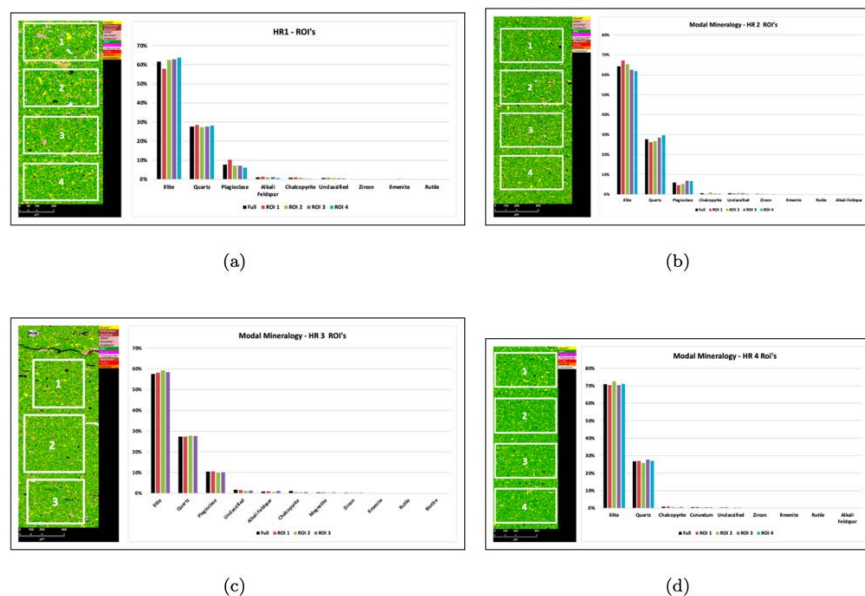


Figure 3: Spatial mineralogy maps, including region of interest areas, from the high-resolution areas. (a) Region 1, (b) Region 2, (c) Region 3, and (d) Region 4.

The four high-resolution regions are similar in terms of rock texture and mineralogy, including the region of interest (ROI) areas analyzed within each of the respective areas. The high-resolution areas are also very similar to the analysis performed on the overview image, indicating a relatively homogenous composition throughout the sample surface.

Table 1: XRD analyses including clay fraction analysis. Values in weight percentages.

Smectite	Ill/Smec	Ill/Mica	Kaolinite	Chlorite	Quartz	Orth	Anh	Albite	Clin	Pyrite	Calcite	Dolomite
22.4	12.3	4.3	0.8	3.9	44.1	3.1	6.0	0.4	0.4	1.1	0.3	0.9

Abbreviations: Ill = Illite, Orth = Orthoclase, Anh = Anhorite, Clin = Clinoptiolite.

The X-ray diffraction (XRD) results of the clay fraction shows that 51.4% of the total clay amount is smectite, 28.1% is mixed layer illite/smectite, 9.8% is illite, 8.9% is chlorite and the remaining is kaolinite. Reichweite from the analysis shows $R=0$, meaning a random mixing of layers in the illite/smectite portion of the clay.

The mineralogy results from both automated spatial mineralogy and XRD are comparable with data found in published research (Zhang et al. [2017]; Wang et al. [2010]; Schultz et al. [1980]). Although the sampled areas and volumes are very small, and published data are recorded from various areas and depths of the Pierre shale, there are strong correlations in terms of overall mineralogy as well as clay composition. In the literature, the amount of clay reported is between 45-75%, where the main component is mixed layer illite/smectite. For quartz the range is 20-45%.

The high-resolution regions are further investigated by acquisition of secondary electron images. In contrast to back-scatter images, secondary electrons originate from the surface or the near-surface regions of the sample. They are a result of inelastic interactions between the primary electron beam and the sample and have lower energy than the back-scattered electrons.

Secondary electrons are very useful for inspection of the topography of the sample surface, in this case for inspection of pores in the sample that are not filled with epoxy (Schieber [2013]; Sondergeld et al.

[2010]). The secondary electron images are acquired at 2500-5000X magnification, and the main objective of these images are to find representative locations for Focused Ion Beam (FIB) image acquisition. Figure 4 shows secondary electron images acquired from high resolution region 2.

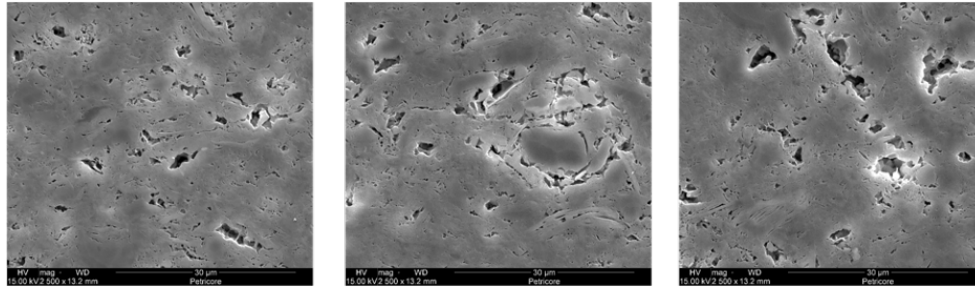


Figure 4: Secondary electron images (SEI) acquired from high resolution region 2

3D reconstructions are made by alternating SEM imaging with FIB milling (Curtis et al. [2012]; Ambrose et al. [2010]). This technique is hence destructive and leaves a milled cavity in the sample. Consecutive slices are aligned and combined into a 3D model. Alignment of the image is further aided by image recognition techniques, focusing on a fixed marking next to where the FIB milling takes place.

FIB-SEM generates a 3D model with an isotropic resolution of 10nm per voxel. The raw data is a 3D data cube of grey levels proportional to the average atomic number of the phase under the electron beam. Heavy phases, such as framboidal pyrites, show up as bright phases while organics are much darker.

Three FIB-SEM images were acquired. The locations for the acquisition of the three images are shown in Figure 5. The locations are selected towards the center of the sample. By selecting locations in the center we have enhanced textural information and generally a better starting point for selecting small volumes ($\approx 20\mu\text{m}$ side lengths) that are representative of the full sample.

Table 2: Size (number of voxels) of the three acquired FIB-SEM images.

Image	n_x	n_y	n_z
FIB1	1979	1454	1070
FIB2	1991	1450	1166
FIB3	1996	1526	1116

Image processing and segmentation of FIB-SEM volumes

The first step of FIB-SEM processing is image enhancement, mainly consisting of alignment of the stack of acquired BSE images followed by feature-preserving noise reduction of the images. The stack alignment is a rigid translation alignment to preserve the continuity of phases in the Z-direction. The image enhancement is demonstrated on a small area of FIB1 in Figure 5, and the enhanced signal-to-noise ratio significantly improves the segmentation of the various phases into a labeled 3D volume.

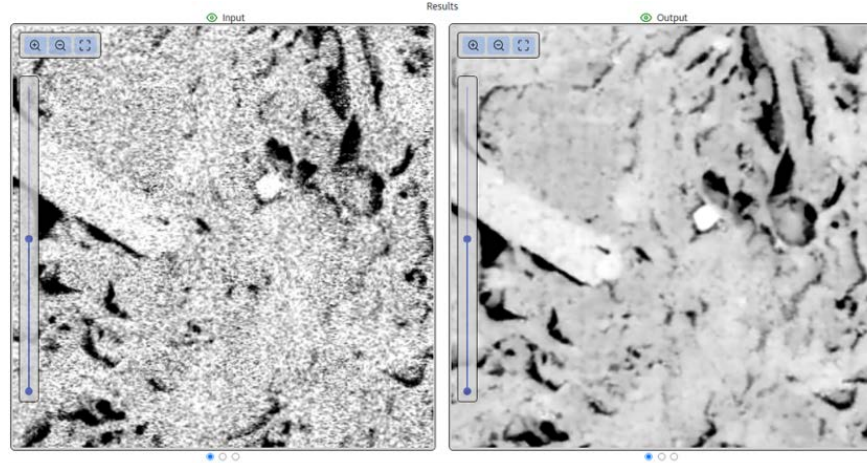


Figure 5: Image enhancement by feature-preserving noise reduction from a small sub-area of FIB1

A common problem in FIB-SEM volumes acquired in tight rocks is the presence of so-called “pore backs”. This occurs when a pore is not deep enough to trap electrons and hence be represented by black pixels. Instead, the electrons bounce off the back of the pore and one observes the underlying mineral where a void space should be (Figure 6). A similar 3D effect can be observed at grain- and pore-edges and can without proper processing result in a significantly under-estimation of the pore space. Due to the pore backs, which visually looks like 3D effects, the typical thresholding of greyscale intensity values cannot be applied directly for accurate results.

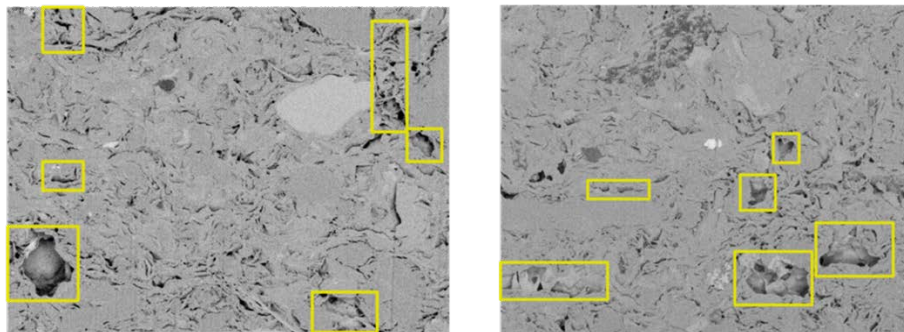


Figure 6: Examples of pore back artefacts observed in FIB1 (a) and FIB2 (b)

Figure 7 shows the multi-step image segmentation workflow that was applied for these 3D volumes. The first step of the segmentation process is to isolate and map the pore backs. This is accomplished by a trainable segmentation tool (Arganda-Carreras et al. [2017]) where the total perimeter of the pore, including pore backs, is initially traced manually. This process is repeated for a range of pores in the volume, and the traced areas are analyzed with respect to properties like shape, structure, gradient, and greyscale mean/variance. The trainable segmentation is an iterative process where the automatic interpretation is enhanced by user-input between each iteration until all the pore backs are mapped completely.

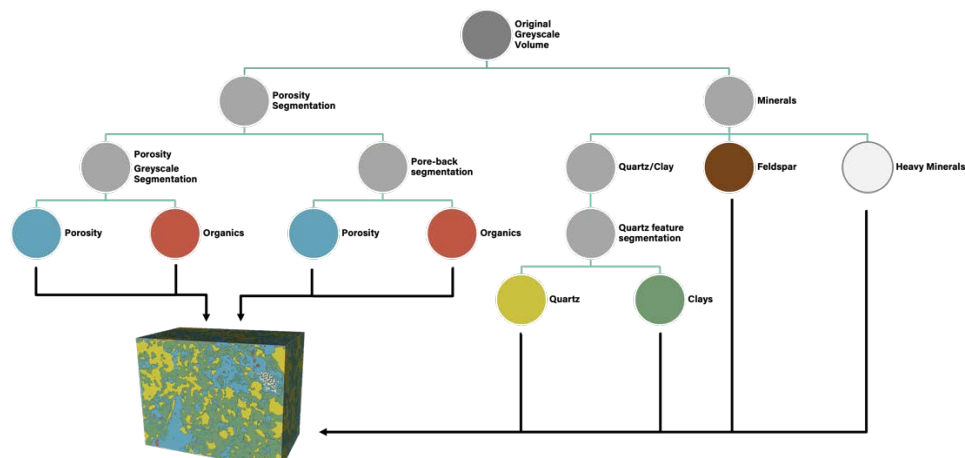


Figure 7: Illustration of the multi-step segmentation workflow

The second step of the segmentation process is to further define the pore space from the rock matrix. This is done by first thresholding of the greyscale intensity values. The porosity mask is then combined with the pore-back mask to produce the final porosity segmentation. An example of the porosity segmentation is shown in Figure 8.

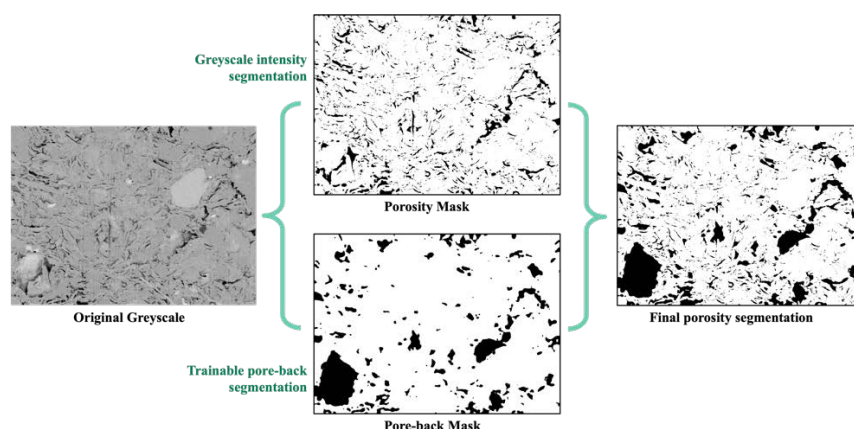


Figure 8: Illustration of the porosity segmentation applied to the FIB-SEM volumes

The third step is a sub-segmentation of the phase initially labeled as rock matrix. The low accelerating voltage required for FIB-SEM acquisition results in very similar greyscale values between clays and grains of various mineralogy. A new set of iterations of the trainable segmentation tool is applied to distinguish the various components of the rock matrix. The morphological distinctiveness is used to differentiate fibrous clay structures from more rounded grains like quartz. These sub-segmentations are applied until the presence of main mineral phases is defined in the 3D volume. All the different segmentations are then merged into a final 3D model that allows for calculations of rock properties. Figure 9 shows the segmented 3D FIB-SEM volumes.

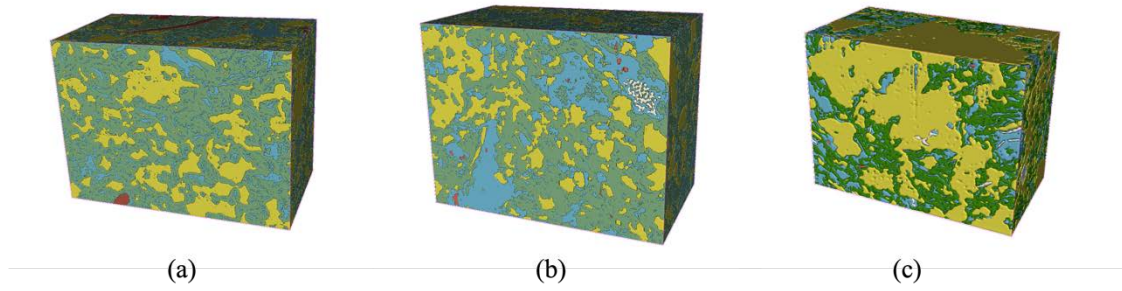


Figure 9: Segmented FIB-SEM volumes. (a) FIB1, (b) FIB2, (c) FIB3. Blue = pore, yellow = quartz, green = clay.

Results

The segmented or resolved porosity (i.e. image porosity at a voxel resolution of 10nm) is denoted ϕ_{res} . The total porosity is denoted ϕ_{tot} and is defined as $\phi_{\text{tot}} = \phi_{\text{res}} + f_c \phi_{\mu}$ where ϕ_{μ} is the clay micro-porosity and f_c is the volume fraction of clay. The total porosity for the plug was measured and reported to be 40.3%. In the digital simulations we used a clay micro-porosity of 40%. This resulted in total porosity values for the FIB-SEM volumes in the range $[34.7\% < \phi_{\text{tot}} < 46.6\%]$, which is in agreement with laboratory measurements.

Table 3: Summary of segmented mineral composition (volume percentage) of the FIB-SEM datasets

Sample	ϕ_{res}	ϕ_{tot}	Clay	Quartz	Feldspar	Organics	Pyrite
FIB1	18.77	39.16	50.99	27.15	3.09	0.0	0.00
FIB2	24.55	46.64	55.23	19.47	0.0	0.57	0.19
FIB3	21.08	34.70	34.05	43.45	0.0	0.18	1.24

Published porosity values for Pierre samples are in the range 25% to 40% (Zhang et al. [2017]; Wang et al. [2010]). These values are high, especially for shales. However, the analyzed FIB-SEM volumes confirm these values. A significant amount of porosity is observed both as relatively large pore bodies and as a network of pores in the clay phase.

Figure 10(a)-(c) show 2D (XY-plane) mineral maps through the 3D segmented FIB-SEM volumes whereas Figure 11(d)-(f) plot the fraction of the main phases (pore, clay, and quartz) for all the XY-slices in the FIB-SEM volumes. The models are clearly heterogeneous, and the amounts of pore, clay, and quartz vary significantly throughout the samples, especially for FIB1 and FIB3. The quartz content for FIB3 is significantly higher than for the other two models.

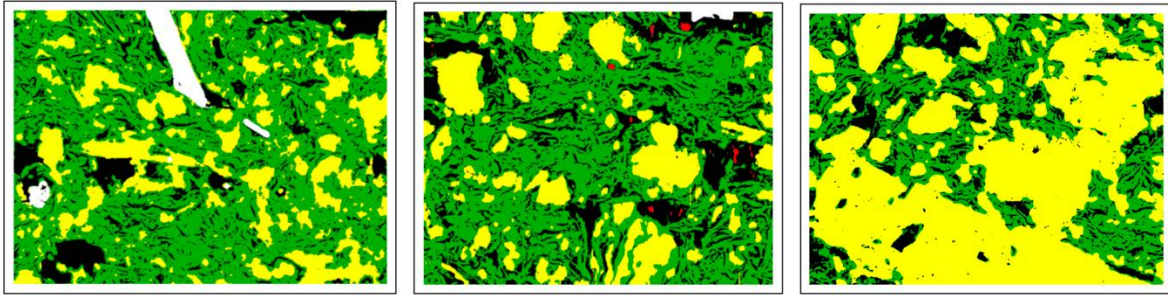


Figure 10: 2D XY-slices illustrating the mineral segmentation. (a) FIB1, (b) FIB2, (c) FIB3. Yellow = quartz, white = feldspar, green = clay, black = pore, red = organics.

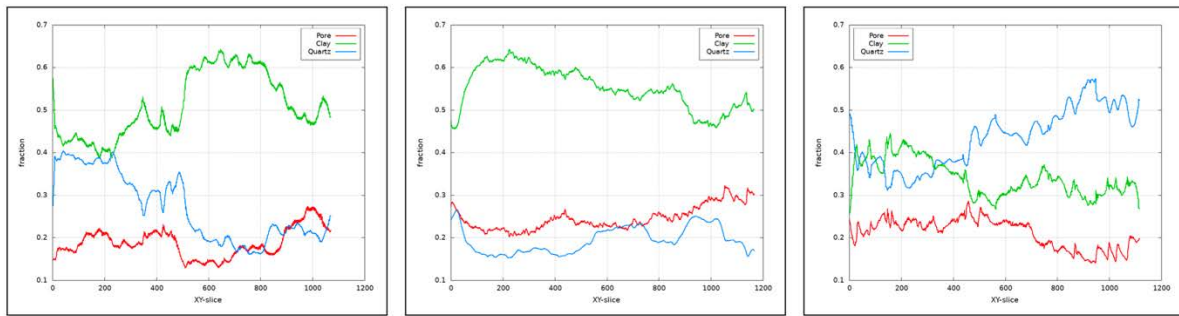


Figure 11: Plotted phase distribution for XY planes throughout each 3D volume. (a) FIB1, (b) FIB2, (c) FIB3.

Basic properties

Absolute permeabilities were calculated by solving the Stokes equations using a no-slip boundary condition at the solid pore walls. Flow through clay-bound water is not accounted for. The contribution of clay-bound water to the absolute permeability is very small since effective permeability is mainly governed by the smallest pore in the percolating backbone of the resolved porosity pore network (Masihi et al. [2016]).

Table 4 summarizes the calculated directional absolute permeabilities (in nano-Darcy) for the three FIB-SEM samples. The calculated permeabilities (i.e. k_x , k_y , k_z) for each sample is fairly isotropic with $k_{i,max}/k_{i,min} < 2$. This is in agreement with the fact that the samples were acquired perpendicular to the bedding plane and no clear indications of lateral heterogeneities were observed. The directionally averaged (arithmetic) permeability k_{avg} is similar for FIB2 and FIB3 (≈ 840 nD). FIB1 has the lowest resolved porosity and also the lowest $k = 120$ nD.

Table 4: Calculated directional permeabilities for the FIB-SEM volumes

Sample	ϕ_{res}	k_x [nD]	k_y [nD]	k_z [nD]	a	b
FIB1	0.188	158	97	106	12.82	5.59
FIB2	0.245	642	640	1185	14.56	4.83
FIB3	0.211	585	960	1020	25.96	3.66

Figure 12 plots directional permeabilities versus porosity for the samples. The cross-plots are generated from permeability calculations on non-overlapping sub-samples from the full FIB-SEM volumes. Sub-

samples indicate the variability of properties within each sample. There is significant spread in permeability at a given porosity, which is due to heterogeneities at the scale of investigation.

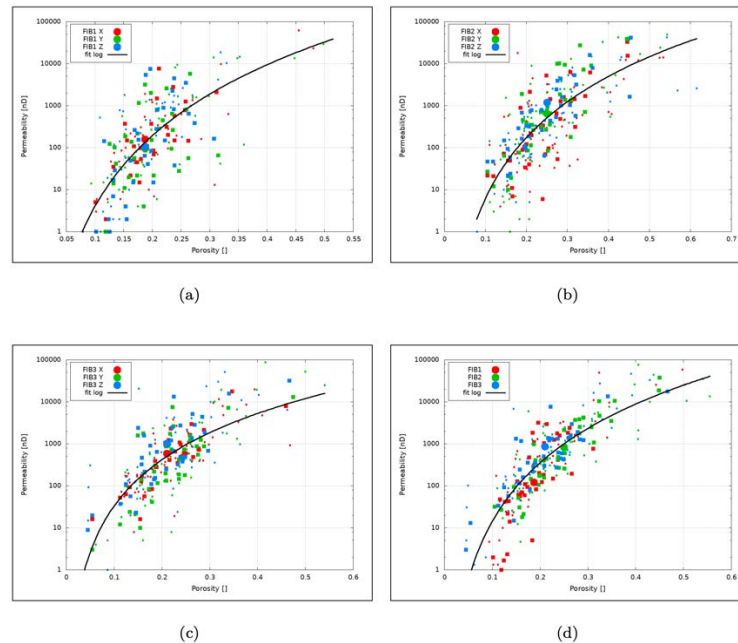


Figure 12: Porosity versus directional permeabilities for the samples. (a) FIB1, (b) FIB2, (c) FIB3, and (d) porosity versus directionally averaged permeability, k_{avg}

A permeability versus porosity correlation of the form $\log k = b \log (a\phi)$ is fitted to the data and is plotted as a black line in Figure 12. Although there are large scatters in the data, especially for the tightest sample FIB1, the correlation appears to capture the general behavior of the simulated permeabilities as a function of porosity. The best-fit values for a and b for each sample are given in Table 4. For the directionally averaged permeability k versus ϕ plot (i.e. Figure 12(d)), the best-fit values are $a = 17.71$ and $b = 4.64$.

Capillary pressure

Capillary pressure curves, $P_c(S_w)$, were calculated by simulating two-phase oil-water primary drainage displacements in the pore network models (PNM) extracted from the segmented FIB-SEM images. The oil-water interfacial tension was set to 30.0 mN/m and the oil and water densities were 700 kg/m³ and 1000 kg/m³, respectively.

Initially, the PNM is filled with water and is strongly water wet having a receding contact angle θ_r randomly distributed in the range $[0^\circ < \theta_r < 10^\circ]$. Oil, the non-wetting phase, then enters the network displacing water. The oil can enter the network from all six faces of the model. This mimics the boundary conditions for mercury injection capillary pressure (MICP) measurements. The clay-bound water is assumed to be impermeable and is not invaded during the simulations.

Figure 13 shows the simulated primary drainage capillary pressure curves for the three FIB-SEM samples. Except for some differences in the irreducible water saturation, S_{wir} , the simulated $P_c(S_w)$ curves are similar. Sample FIB1 has the highest S_{wir} . It is also the sample with the lowest resolved porosity and permeability. The S_{wir} is mainly due to isolated or shielded resolved porosity, in example porosity which can only be invaded via clay-bound water.

The entry capillary pressure, p_{ct} , is similar for the three samples ($p_{ct} \approx 1$ bar). There is no plateau region observed in the $P_c(S_w)$ curves and the capillary pressure increases almost linearly over a large saturation

range, suggesting a fractal pore-size distribution. The simulated $P_c(S_w)$ curves were fitted to the Brooks-Corey capillary pressure model (Brooks and Corey [1966])

$$P_c = p_{ct}(S_{wN})^{-1/\lambda}$$

where S_{wN} is the normalized water saturation and λ is the pore size distribution index which is related to the fractal dimension (Li [2004]) $D_f = 3 - \lambda$. D_f is a representation of the heterogeneity of the sample. The greater the fractal dimension, the greater the heterogeneity. The calculated fractal dimension for the samples were in the range $[1.6 < D_f < 2.1]$. FIB1 has the largest D_f and FIB3 the smallest.

Capillary pressure curves are often used to characterize the pore size distribution (psd) of porous rocks. The pore size distribution is calculated from $dS_w/d(\ln(P_c))$ using equal logarithmically spaced capillary pressure pressure steps. However, it is well known that capillary pressure data do not lead to the true pore size distribution but to the distribution controlled by pore throat thresholds of size r_t .

Figure 13(c) shows the pore throat radius distributions derived from the simulated capillary pressure data. The samples have a broad pore size distribution covering more than two orders of magnitude. The pore size distributions for samples FIB2 and FIB3 are similar with the peak in the distribution occurring at $r_t \approx 45\text{nm}$. The peak for sample FIB1 occurs at smaller pore sizes, $r_t \approx 28\text{nm}$. This explains the lower permeability of FIB1 (see Table 4).

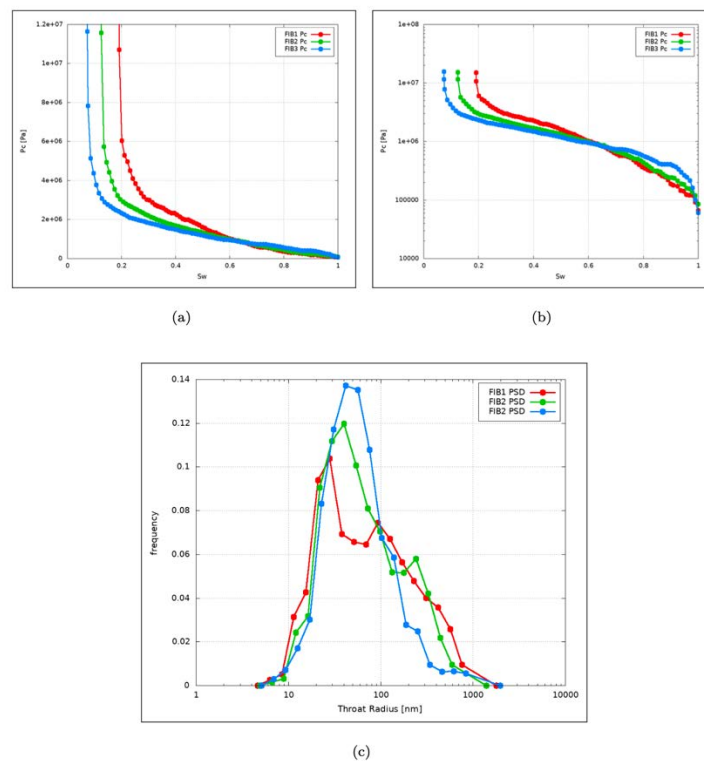


Figure 13: Simulated primary drainage capillary pressure curves; (a) linear-linear plot, and (b) semi-logarithmic plot. (c) Pore throat size distribution derived from the capillary pressure data.

Elastic properties

To simulate the elastic behavior of shale, the elastic properties of individual rock components are required. Whereas the elastic properties of pure minerals such as quartz, feldspar, kaolinite, etc., have been published, the elastic properties of a mixture of clay minerals are also needed.

The clay phase is modeled as an assembly of locally aligned clay platelets (Sayers and den Boer [2018]). The small void spaces or micro-porosity (ϕ_μ) between the platelets contain clay-bound water. The mineral composition of generalized clay platelets for numerical calculations is given by the XRD data (see Table 1). The effective elastic properties of the clay platelets are derived from the constituent clay minerals (see Table 5) using the Voigt-Reuss-Hill averaging method (Mavko et al. [2009]).

Table 5: Elastic moduli from the constituent clay minerals. The elastic moduli of the clay platelet are calculated from mixing laws whereas properties for the clay phase are derived using DEM theory.

Clay Mineral	fraction	K [GPa]	G [GPa]	ρ [g/cm ³]
Smectite	0.514	9.3	6.9	2.61
Mixed Layer 1 (smectite/illite)	0.281	12.7	8.5	2.63
Mixed Layer 2 (illite/mica)	0.098	41.4	22.0	2.75
Kaolinite	0.018	7.9	10.2	2.44
Chlorite	0.089	164.3	51.4	2.84
Clay platelet		19.6	10.7	2.65
Clay phase ($\phi_\mu = 40\%$)		8.4	4.1	1.99

The effective elastic moduli for the clay phase (platelet + micro-porosity) are calculated using differential effective medium (DEM) theory (Norris et al. [1985]; Berryman [1992]). The clay platelets are considered to be the background medium with spherical and plate-like inclusions of water filled void space. The clay micro-porosity is estimated to be $\phi_\mu \approx 40\%$. A fourth order Runge-Kutta method is used to solve the DEM equations. Table 6 summarizes the elastic input parameters used for the simulations. The elastic moduli for pure minerals and organics are published data (Mavko et al. [2009]; Zhao et al. [2016]). The pore phase is fully brine saturated and the elastic moduli are those of water.

Table 6: Input bulk modulus, shear modulus and density for the phases used in the calculations

Phase	K [GPa]	G [GPa]	ρ [g/cm ³]
Pore	2.2	0.0	1.00
Clay	8.4	4.1	1.99
Quartz	37.0	44.0	2.65
Feldspar	37.5	15.0	2.61
Organics	3.5	1.75	1.10
Pyrite	147.4	132.5	4.90

We calculated elastic properties for two symmetry cases: (i) no symmetry, and (ii) isotropic symmetry. The no-symmetry case has 21 independent elastic constants compared to 2 for the isotropic one. The simulations for case (i) are therefore significantly more time consuming.

The computed effective elastic properties for the entire sample sizes are summarized in Table 7. The calculations are representing fully brine saturated samples. Sample FIB3 is more quartz-rich (see Table 3) and it has the largest effective bulk and shear modulus and P - and S -wave velocities. FIB2 has the highest

porosity, and it has the lowest elastic moduli and velocities. For all three samples, the results for the isotropic and no-symmetry cases are close, suggesting that the isotropic symmetry assumption is a good engineering approximation for these samples. FIB3 displays the largest difference between the two symmetry cases. This is probably due to the presence of a large quartz grain that extends across the entire FIB-SEM volume (see Figure 10 (c)).

Table 7: Calculated effective elastic properties on the full sample sizes for the no-symmetry and isotropic symmetry cases

Symmetry	Sample	ρ [g/cm ³]	K [GPa]	G [Gpa]	V _p [km/s]	V _s [km/s]
no-symmetry	FIB1	2.00	9.47	4.82	2.82	1.55
no-symmetry	FIB2	1.87	7.21	2.98	2.44	1.26
no-symmetry	FIB3	2.10	11.65	7.15	3.18	1.84
isotropic	FIB1	2.00	9.26	4.97	2.81	1.57
Isotropic	FIB2	1.87	6.92	2.93	2.40	1.25
isotropic	FIB3	2.10	11.08	6.57	3.07	1.77

Results for the elastic properties include simulations on non-overlapping sub-samples. Isotropic symmetry was assumed for these calculations. Sub-sample calculations indicate the variability in properties contained in each sample. The calculated elastic properties are presented in Figure 14. The data is plotted as a function of the total porosity ϕ_{tot} which is defined as

$$\phi_{\text{tot}} = \phi_{\text{res}} + \phi_{\mu} f_{\text{clay}}$$

where f_{clay} is the volume fraction of clay. The trends plotted against total porosity are close to linear with a larger scatter at low and high porosities.

Figure 15 shows the composite or global trends of elastic properties versus total porosity from all three samples. In the range $[0.25 < \phi_{\text{tot}} < 0.55]$ we observe a strong correlation of the properties with total porosity. At low and high ϕ_{tot} the best fit linear correlations, plotted as a black line, underestimate the elastic properties.

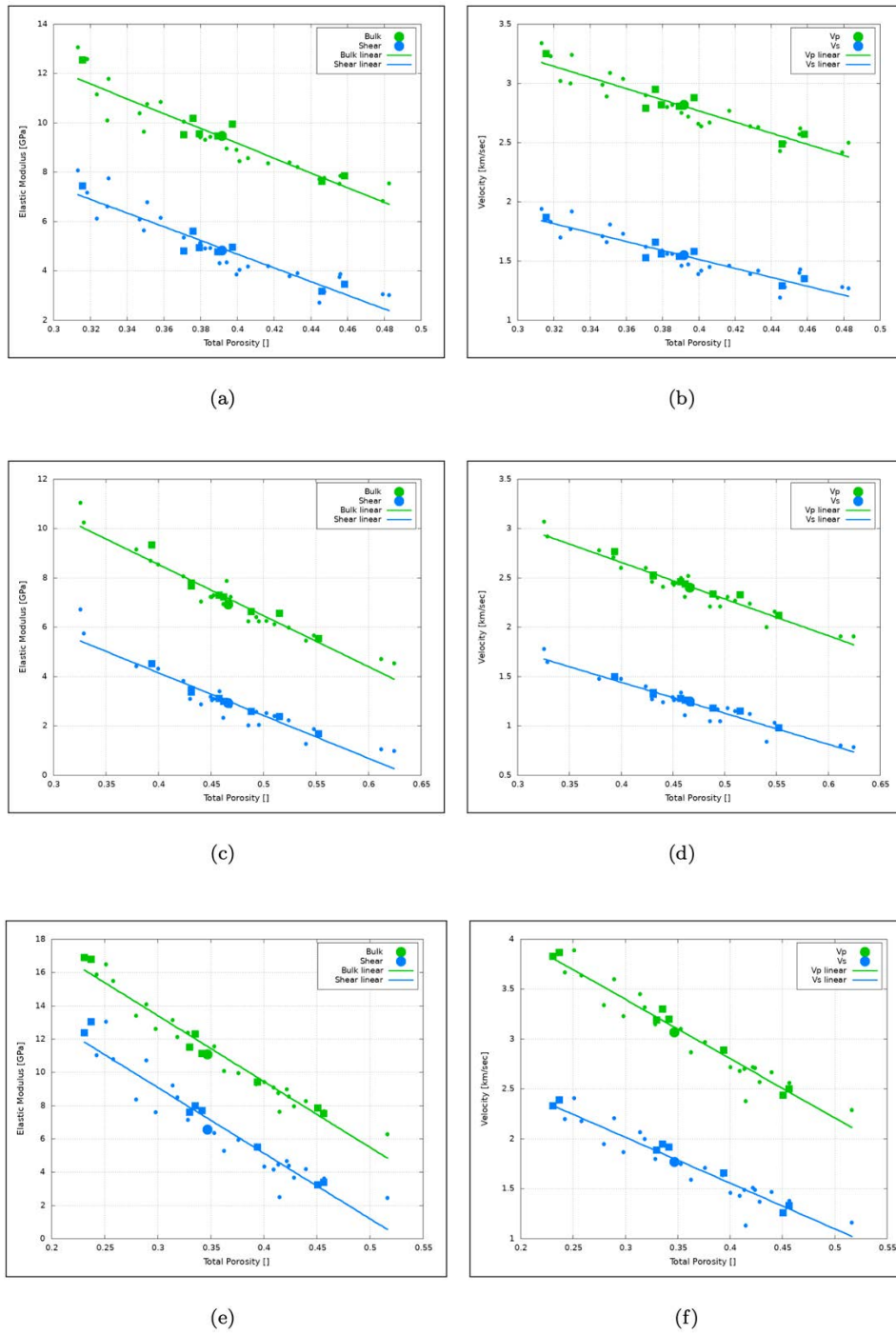


Figure 14: Elastic properties versus total porosity trends calculated on sub-samples. (a, b) FIB1, (c, d) FIB2, and (e, f) FIB3

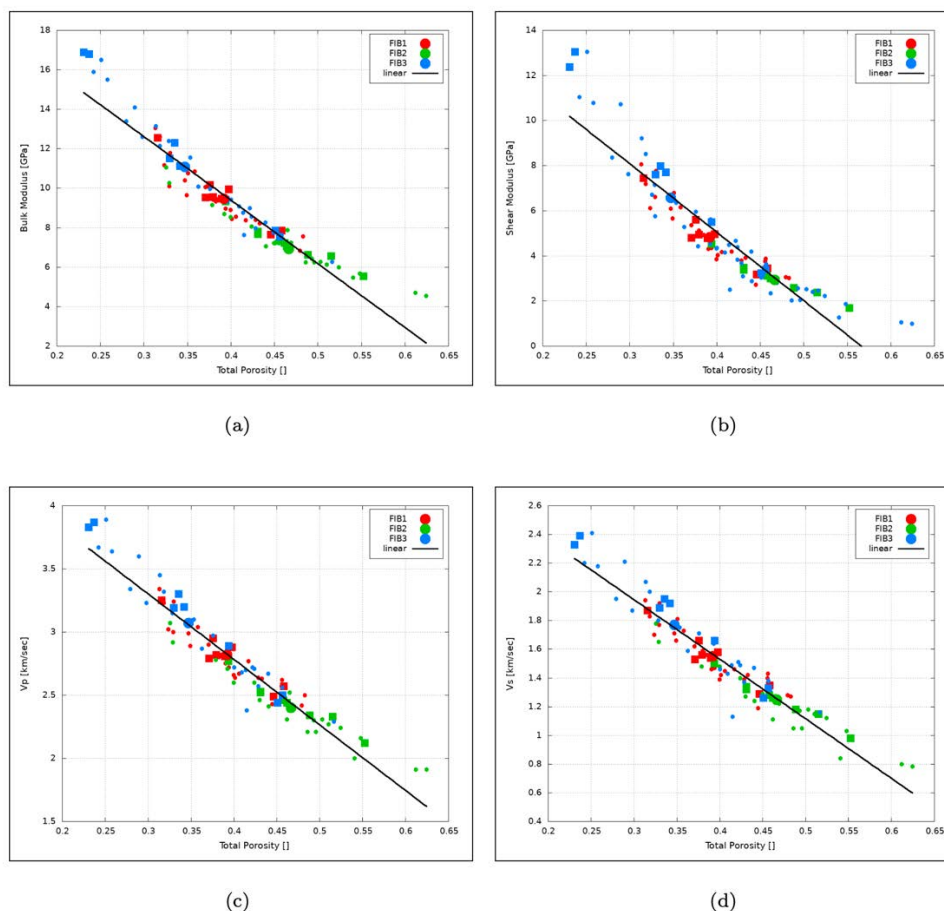


Figure 15: Composite trends of elastic properties versus total porosity for the three FIB-SEM volumes. (a) Bulk modulus, K , (b) Shear modulus, G , (c) Bulk velocity, V_p , (d) Shear velocity, V_s

Discussion

The digital multi-modal and multi-scale methodology for deriving advanced properties from small sample volumes appear to yield very encouraging results. The systematic imaging workflow, by acquisition of multi-modal image pyramids, is continuously evaluated and tuned to ensure representative areas are selected as the workflow progresses. Combining qualitative and quantitative data through SEM images and spatial mineral maps is valuable for the sub-sampling process, but is also of high importance for comparison of results derived from a novel methodology with results reported from laboratory experiments.

The refined image processing and segmentation workflow facilitates the generation of a digital model of the acquired FIB-SEM images. A feature-preserving noise reduction filter significantly improves the signal-to-noise ratio, which is important for labeling the various phases as well as preserving continuity of the respective phases in three dimensions. Trainable segmentation algorithms have been applied to successfully capture the pore space that is typically difficult to accurately characterize due to pore backs. A similar workflow was performed to separate the various mineralogical components that are initially labeled as the rock matrix.

The segmented 3D volumes are, together with clay fraction analysis from XRD, used for calculation of elastic properties. The elastic moduli of the clay platelets are calculated from mixing laws whereas

properties for the clay phase are derived using DEM theory. The clay platelets are considered to be the background medium, modeled as assemblies of locally aligned clay platelets, with a clay micro-porosity estimated to be 40%. The calculations, representing fully brine saturated samples, show a strong correlation of properties with total porosity in the range [$25\% < \phi_{\text{tot}} < 50\%$].

Elastic properties, as well as petrophysical properties, derived from digital rock analysis are in good agreement with both laboratory measured data and properties found in literature. Further comparisons and evaluations will be conducted as supplementary experimental data become available.

The agreement in results is encouraging for the application of this methodology on drill cuttings. The main alteration in a similar workflow for drill cuttings is the replacement of an overview image with spatial mineralogy of a relatively large sample surface with multiple ROI analyses covering a selection of drill cuttings. Characterization and rock typing of the cuttings will be essential for identifying representative locations for acquisition of high-resolution 3D volumes.

Acknowledgements

This work has been made possible through the research project “Advanced laboratory methods for cuttings analyses (Cutting Edge)”, financed by The Research Council of Norway (Project no. 280942).

References

- Ray J. Ambrose, Robert C. Hartman, Mery Diaz-Campos, I. Yucel Akkutlu, and Carl H. Sondergeld. 2010. New Pore-scale Considerations for Shale Gas in Place Calculations. SPE Unconventional Resources Conference / Gas Technology Symposium. SPE-131772-MS.
- Ignacio Arganda-Carreras, Verena Kaynig, Curtis Rueden, Kevin W Eliceiri, Johannes Schindelin, Albert Cardona, and H Sebastian Seung. 2017. Trainable Weka Segmentation: a machine learning tool for microscopy pixel classification. *Bioinformatics*, 33(15):2424–2426.
- J.G. Berryman. 1992. Singel-scattering approximation for coefficients in biot’s equations of poroelasticity. *J. of the Acoustical Society of America*, 91:551–571. doi: 10.1121/1.402518.
- Craig M. Bethke and Stephen P. Altaner. 1986. Layer by layer mechanism of smectite illitization and application to a new rate law. *Clays and Clay Minerals*, 34:136–145.
- R.H Brooks and A.T. Corey. 1966. Properties of porous media affecting fluid flow. *Journal of the Irrigation and Drainage Division*, 92:61–90.
- Mark Curtis, Carl Sondergeld, Raymond Ambrose, and Chandra Rai. 2012. Microstructural investigation of gas shales in two and three dimensions using nanometer scale resolution imaging. *AAPG Bulletin*, 96:665–677.
- E.J. Garboczi and A.R. Day. 1996. An algorithm for computing the effective linear elastic properties of heterogenous materials: Three dimesnional results for composites with equal phase poisson ratios. *Journal of the Mechanics and Physics of Solids*, 43:1349–1362. doi: 10.1016/0022-5096(95) 00050-5.
- David Katz, Marshall Jung, Lyn Canter, Mark Sonnenfeld, Mark Odegard, John Daniels, Alan Byrnes, Mary Guisinger, Kim Jones, and John Forster. 2016. Mineralogy Derived Brittleness from the Qemscan: Niobrara Case Study. SPE-180251-MS.

Herman Lemmens, Eric Goergen, Kimball Skinner, and Michael Owen. 2013. From SEM Maps and EDS Maps to Numbers in Unconventional Reservoirs. Unconventional Resources Technology Conference. doi: 10.1190/urtec2013-179. URL <https://doi.org/10.1190/urtec2013-179>.

K. Li. 2004. Generalized capillary pressure and relative permeability model inferred from fractal characterization of porous media. SPE 89874.

Robert Loucks, Robert Reed, Stephen Ruppel, Daniel And, and Daniel Jarvie. 2009. Morphology, genesis, and distribution of nanometer-scale pores in siliceous mudstones of the mississippian barnett shale. *Journal of Sedimentary Research*, 79:848–861, 11.

M. Masihi, P.A. Gago, and P.R. King. 2016. Estimation of the effective permeability of heterogeneous porous media by using percolation concepts. *Transport in Porous Media*, 114:169–199.

G. Mavko, T. Mukerji, and J. Dvorkin. 2009. *The rock physics handbook*. Cambridge University Press.

R.P. Mayer and R.A. Stowe. 1965. Mercury porosimetry-breakthrough pressure for penetration between packed spheres. *J. Colloid Interface Sci.*, 20:893–911.

Duane Milton Moore and Robert C Reynolds. 1989. *X-ray Diffraction and the Identification and Analysis of Clay Minerals*. Oxford University Press.

A. Norris, A. Callegari, and P. Sheng. 1985. A generalized differential effective medium theory. *J. of The Mechanics and Physics of Solids*, 33:525–543. doi: 10.10616/0022-5096(85)90001-8.

P.E. Øren and S. Bakke. 2003. Reconstruction of Berea sandstone and pore-scale modelling of wettability effects. *Journal of Petroleum Science and Engineering*, 39:177–199.

P.E. Øren, S. Bakke, and O.J. Arntzen. 1998. Extending predictive capabilities to network models. *SPE Journal*, 3:324–336.

P.E. Øren, L.C. Ruspini, M. Saadatfar, R.M. Sok, and A. Herring. 2019. In-situ pore-scale imaging and image-based modelling of capillary trapping for geological storage of CO₂. *International Journal of Greenhouse Gas Control*, 87:34–43. doi: 10.1016/j.ijggc.2019.04.017.

Richard M. Pollastro. 1993. Considerations and applications of the illite/smectite geothermometer in hydrocarbon-bearing rocks of miocene to mississippian age. *Clays and Clay Minerals*, 41:119–133.

J. Poutet, D. Manzoni, F. Hage-Chehade, J.F. Tovert, and P.M. Adler. 1996. The effective mechanical properties of random porous media. *Journal of the Mechanics and Physics of Solids*, 44:1587–1620. doi: 10.1016/0022-5096(96)00051-8.

H.M. Princen. 1969. Capillary phenomena in assemblies of parallel cylinders. i. capillary rise between two cylinders. *J. Colloid Interface Sci.*, 30:69–75.

L.C. Ruspini, R. Farokhpoor, and P.E. Øren. 2017. Pore-scale modeling of capillary trapping in water-wet porous media: A new cooperative pore-body filling model. *Advances in Water Resources*, 108:1–14.

L. Santoro, Gavyn Rollinson, Maria Boni, and Nicola Mondillo. 2015. Automated scanning electron microscopy-based mineral identification and quantification of the jabali zn pb ag nonsul- fide deposit (Yemen). *Economic Geology*, 110:1083–1099.

C.M Sayers and L.D. den Boer. 2018. The elastic properties of clay in shales. *J. of Geophysical Reserach: Solid Earth*, 123:5965–5974. doi: 10.1029/2018JB015600.

Juergen Schieber. 2013. 13 sem observations on ion-milled samples of Devonian black shales from Indiana and New York, the petrographic context of multiple pore types. In *Electron Microscopy of Shale Hydrocarbon Reservoirs*. American Association of Petroleum Geologists.

L. G. Schultz, H. Allison Tourtelot, J. R. Gill, and J. G. Boerngen. 1980. Composition and properties of the pierre shale and equivalent rocks, northern great plains region.

Carl Sondergeld, Raymond Ambrose, Chandra Rai, and Jason Moncrieff. 2010. Microstructural studies of gas shales. *Annual Society of Petrophysicists and Well Log Analysts Symposium*, 02.

S. Torquato. 2002. *Random Heterogenous Materials*. Springer-Verlag.

D. Wang, R. Butler, H. Liu, and S. Ahmed. 2010. Flow Rate Behavior and Imbibition in Shale

D. Wilkinson and J.F. Willemsen. 1983. Invasion percolation: a new form of percolation theory. *Journal of Physics A*, 16:3365–3376. doi: 10.1088/0305-4470/16/14/028.

Z. Yan, X. Yang, S. Li, and M. Hilpert. 2017. Two-relaxation-time lattice boltzmann method and its application to advective-diffusion-reactive transport. *Advances in Water Resources*, 109:333–342. doi: 10.1016/j.advwatres2017.09.003.

C. Zhang, R. Pathegama Gamage, and J. Zhao M. Perera. 2017. Characteristics of clay-abundant shale formations use of co2 for production enhancement. *Energies*, 10:1887–.

L. Zhao, X. Quin, D.H. Han, J. Geng, and Z. Yang. 2016. Rock-phusics modeling for the elastic properties of organic shale at different maturity stages. *Geophysics*, 81:527–541. doi: 10.1190/geo2015-0713. 1.